Alternating block copolymer-based nanoparticles as tools to modulate the loading of multiple chemotherapeutics and imaging probes

Acta Biomaterialia 80 (2018) 341–351

Contents lists available at ScienceDirect

Acta Biomaterialia

journal homepage: www.elsevier.com/locate/actabiomat

Full length article

Alternating block copolymer-based nanoparticles as tools to modulate the loading of multiple chemotherapeutics and imaging probes

C. Mattu [a,f,*,1], G. Brachi [a,f,1], L. Menichetti [b,c], A. Flori [c], P. Armanetti [b], E. Ranzato [d], S. Martinotti [e], S. Nizzero [f,g], M. Ferrari [f,h], G. Ciardelli [a]

[a] Politecnico di Torino, DIMEAS C.so Duca degli Abruzzi 24, 10129 Torino, Italy
[b] Institute of Clinical Physiology, National Research Council, Via G. Moruzzi, 1 56124 Pisa, Italy
[c] Fondazione Regione Toscana G. Monasterio, Via Giuseppe Moruzzi 1, Pisa 56124, Italy
[d] DiSIT-Dipartimento di Scienze e Innovazione Tecnologica, University of Piemonte Orientale, piazza Sant'Eusebio 5, Vercelli 13100, Italy
[e] DiSIT-Dipartimento di Scienze e Innovazione Tecnologica, University of Piemonte Orientale, Viale Teresa Michel 11, Alessandria 15121, Italy
[f] Department of Nanomedicine, Houston Methodist Hospital Research Institute, Houston, TX 77030, USA
[g] Applied Physics Graduate Program, Smalley-Curl Institute, Rice University, Houston, TX 77005, USA
[h] Department of Medicine, Weill Cornell Medical College, New York, NY 10065, USA

ARTICLE INFO

Article history:
Received 17 May 2018
Received in revised form 30 August 2018
Accepted 15 September 2018
Available online 18 September 2018

ABSTRACT

Cancer therapy often relies on the combined action of different molecules to overcome drug resistance and enhance patient outcome. Combined strategies relying on molecules with different pharmacokinetics often fail due to the lack of concomitant tumor accumulation and, thus, to the loss of synergistic effect. Due to their ability to enhance treatment efficiency, improve drug pharmacokinetics, and reduce adverse effects, polymer nanoparticles (PNPs) have been widely investigated as co-delivery vehicles for cancer therapies. However, co-encapsulation of different drugs and probes in PNPs requires a flexible polymer platform and a tailored particle design, in which both the bulk and surface properties of the carriers are carefully controlled. In this work, we propose a core-shell PNP design based on a polyurethane (PUR) core and a phospholipid external surface. The modulation of the hydrophilic/hydrophobic balance of the PUR core enhanced the encapsulation of two chemotherapeutics with dramatically different water solubility (Doxorubicin hydrochloride, DOXO and Docetaxel, DCTXL) and of Iron Oxide Nanoparticles for MRI imaging. The outer shell remained unchanged among the platforms, resulting in un-modified cellular uptake and in vivo biodistribution. We demonstrate that the choice of PUR core allowed a high entrapment efficiency of all drugs, superior or comparable to previously reported results, and that higher core hydrophilicity enhances the loading efficiency of the hydrophilic DOXO and the MRI contrast effect. Moreover, we show that changing the PUR core did not alter the surface properties of the carriers, since all particles showed a similar behavior in terms of cell internalization and in vivo biodistribution. We also show that PUR PNPs have high passive tumor accumulation and that they can efficient co-deliver the two drugs to the tumor, reaching an 11-fold higher DOXO/DCTXL ratio in tumor as compared to free drugs.

Statement of Significance

Exploiting the synergistic action of multiple chemotherapeutics is a promising strategy to improve the outcome of cancer patients, as different agents can simultaneously engage different features of tumor cells and/or their microenvironment. Unfortunately, the choice is limited to drugs with similar pharmacokinetics that can concomitantly accumulate in tumors. To expand the spectrum of agents that can be delivered in combination, we propose a multi-compartmental core-shell nanoparticles approach, in which the core is made of biomaterials with high affinity for drugs of different physical properties. We successfully co-encapsulated Doxorubicin Hydrochloride, Docetaxel, and contrast agents and achieved a significantly higher concomitant accumulation in tumor versus free drugs, demonstrating that nanoparticles can improve synergistic cancer chemotherapy.

* Corresponding author.
[1] Shared first authorship.

https://doi.org/10.1016/j.actbio.2018.09.021
1742-7061/

1. Introduction

Efficient cancer treatment requires the drug to be delivered in the right time and at the right place to maximize efficacy and minimize off-target side effects [1]. Because of the ability of cancer cells to become resistant to treatments through the acquisition of sequential mutations, the synergistic action of multiple drugs is often manipulated to improve the therapeutic outcome of cancer patients. Such combined strategies heavily rely on different drugs reaching the same target at the same time, posing the issue of their co-localization at the tumor site [2]. Indeed, different molecules may not reach the tumor concomitantly due to their different physical/chemical properties, administration routes and pharmacokinetics, resulting in the loss of synergistic effect [3,4].

Nanotechnology has provided several platforms designed to package different molecules and/or imaging probes in an all-in-one system in the attempt to enhance their co-delivery to the tumor area [5–7]. Among them, polymer nanoparticles (PNPs) have emerged as powerful tools, in virtue of their low toxicity profile, enhanced tumor accumulation through passive and active targeting mechanisms, reduced renal clearance, and ability to co-host multiple drugs [6,8]. For instance, Blanco and co-workers demonstrated that drug co-encapsulation is a key factor to exploit synergy in vivo. They achieved a significantly higher reduction of tumor volume when using Poly(ε-caprolactone) (PCL) nanoparticles to co-deliver Rapamycin and Paclitaxel to breast cancer as compared to single-agent platforms [3]. Stigliano et al. also enhanced the effect of Docetaxel by co-loading this drug and the chemo-sensitizer Curcumin into poly(D,L) lactide-co-glycolide (PLGA) nanoparticles [9]. The above studies demonstrate that hydrophobic polymer matrices are powerful tools to synergize hydrophobic drugs with high entrapment efficiency. Nevertheless, concomitant chemotherapy with agents of different chemical/physical properties remains a challenge as it requires to design biomaterials with high affinity for both drugs.

In this work we exploit the versatile chemistry of polyurethanes (PURs) to synthesize three polymers with modulated hydrophilic/hydrophobic balance, achieved by inserting randomly-distributed hydrophobic (PCL) and hydrophilic (PEG) domains at different ratios [10–13]. Our previous papers, demonstrated that PURs are promising candidates for the encapsulation of hydrophobic drugs. For instance we showed that these polymers have a 3 fold-higher Paclitaxel encapsulation efficiency as compared to polyester nanoparticles and are able to sustain drug release for a longer period of time [11].

Here we investigated the effect of the PUR core composition on the co-encapsulation of three agents: two potent chemotherapeutics with different water solubility and biodistribution profiles (i.e. Docetaxel and Doxorubicin Hydrochloride) and Superparamagnetic Iron Oxide nanoparticles (SPIOs) for magnetic resonance imaging (MRI). [14–16]. Because the use of different polymers may modify the surface properties of PNPs, and in turn affect their biodistribution and clearance, we opted for a core-shell design to exploit the polymer properties only for the purpose of maximizing payload encapsulation without altering the surface compartment and, consequently, maintaining the same in vivo biodistribution [17–19]. The schematic representation of the PUR PNPs is reported in Fig. 1: all particles have the same phospholipid outer shell and a different PUR core with modulated hydrophilic/hydrophobic balance, obtained by varying the ratio between hydrophilic and hydrophobic blocks in the PUR composition. We also investigated the possibility of combining different imaging modalities such as photo acoustic imaging (PAI) and MRI in the same platform, by coupling a near infrared (NIR) dye to the amine-terminated PEG chains on the phospholipid outer compartment to merge the anatomical, morpho-functional and metabolic information of PAI, with the depth of investigation achievable with MRI for a more comprehensive diagnosis [20–23].

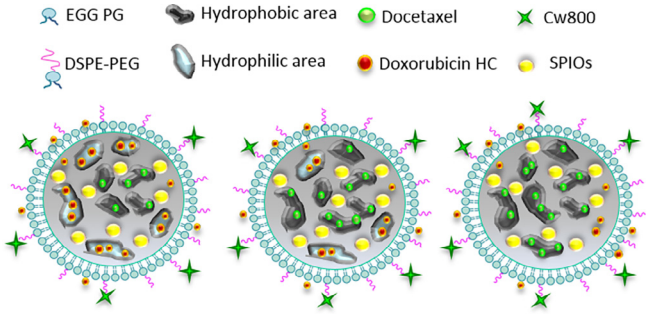

Fig. 1. Schematic representation of nanoparticles prepared with polyurethanes with a different hydrophilic/hydrophobic balance. The lipid shell is composed by a combination of two different phospholipids: L-α-phosphatidylglycerol (EGG-PG) and 1,2-distearoyl-sn-glycero-3-phosphoethanolamine-N-[amino(polyethyleneglycol)-2000] (DSPE-PEG).

We show that the hydrophilic/hydrophobic balance within the PUR core affects the encapsulation and release of the hydrophilic Doxorubicin HC, while plays a minor role on the release kinetics of Docetaxel. It also strongly influences the entrapment of SPIOs and, consequently the MRI contrast enhancement. In addition, we demonstrate that the core shell approach allows modulation of the core properties, while un-altering the surface and thus maintaining the same cell internalization, in vivo biodistribution profile and PAI performances. Moreover, we tested the best-performing particles in tumor-bearing mice obtaining a high passive tumor accumulation, where up to 30% of the circulating particles accumulate in the tumor after 24 h. The co-loaded platform successfully delivered the two drugs to the tumor, achieving a 17-fold and a 1.6-fold higher drug accumulation for Doxorubicin HC and Docetaxel respectively, as compared to the free-drug combination.

2. Materials and methods

2.1. Materials

For PUR synthesis: Poly(ε-caprolactone)-diol (PCL-diol (2,000 g/mol), Poly(ethylenglicole) (PEG (2,000 g/mol), n-BOC Serinol, Dibutyl Dilaurate (DBTL), and 1,6 Hexamethylene diisocyanate (HDI) were purchased from Sigma Aldrich (Italy). L-α-phosphatidylglycerol (EGG-PG), 1,2-distearoyl-sn-glycero-3-phosphoethanolamine-N-[amino(polyethyleneglycol)-2000] (DSPE-PEG-NH_2) and L-α-Phosphatidylethanolamine-N-(lissamine-rhodamineB-sulfonyl) (Egg-Liss-Rhod PE) were purchased from Avanti Polar Lipids. The NIR dye CW800-NHS ester was purchased from Li-cor. SPIOs (5 nm), Doxorubicin Hydrochloride, Docetaxel and all cell culture reagents were purchased from Sigma Aldrich (Italy). All solvents were of analytical grade. Balb/c mice were purchased from Charles River laboratories (USA). Animal studies were conducted under the approval of the Animal Care and Use Committee at the Houston Methodist Research Institute, in adherence to the National Institutes of Health Guide for the Care and Use of Laboratory Animals.

2.2. Polyurethane synthesis

PURs synthesis was carried out following a two-step synthesis procedure in inert atmosphere, by dissolving PCL-diol (for

PCL-based polyurethane, PU100) or a mixture of PCL-diol and PEG (for mixed PCL-PEG polyurethanes, PU70 and PU80) in anhydrous 1,2-dichloroethane (DCE) (20% w/v) [11]. Diisocyanate (HDI) was added at 2:1 M ratio and the reaction was allowed to proceed for 150 min at 85 °C to obtain a pre-polymer (DBTL was used in catalytic amount), followed by n-BOC serinol chain extender addition (1:1 M ratio) at room temperature. The chain extension reaction was stopped after 16 h by addition of methanol, the polymer was precipitated in petroleum ether, and purified by precipitation in diethyl-ether/methanol (95:5) to remove low molecular weight impurities and residual catalyst. Size exclusion chromatography (SEC, Agilent Technologies 1200 Series, USA) was used to determine PUR molecular weight using a Refractive Index detector and two Waters Styragel columns (HT2 and HT4) conditioned at 35 °C. Tetrahydrofuran was used as mobile phase at a flow rate of 0.5 mL/min with an injection volume of 20 μL. Attenuated Total Reflectance Fourier Transform Infrared Spectroscopy (ATR-FT-IR) was performed using a Perkin Elmer Spectrum 100 equipped with an ATR accessory (UATR KRS5) with diamond crystal.

2.3. Preparation of hybrid PUR/lipid nanoparticles

Nanoparticles were prepared by a nanoprecipitation/self-assembly method. Doxorubicin HC (DOXO, 50 μg), SPIOs (100 μg) and PURs were dissolved in chloroform and the solvent was allowed to completely evaporate under nitrogen flow. The polymer/DOXO/SPIOs precipitate was solubilized in a 1 mL solution of Docetaxel (DCTXL, 100 μg) in acetonitrile. The solution was then dropped into 2 mL of water containing 200 μg of Egg-PG and 240 μg of DSPE-PEG-NH_2 and 100 μg of CW800-DSPE-PEG at 60 °C. Following addition of DI water (1 mL) the particle suspension was centrifuged at 3200 rpm and washed twice using a solution concentrator with a molecular-weight cutoff of 10 kDa. For cell internalization studies, drug-free Rhodamine-labeled nanoparticles were prepared by adding 5 μg of Egg Liss Rhod PE in water during nanoparticles preparation.

2.4. Physico-chemical characterization of nanoparticles

The particle size and size distribution were analyzed using Dynamic Laser light Scattering (DLS) (Malvern, Zetasizer Nano S90) on three independent PNPs batches. For morphological analysis, transmission electron microscopy (TEM) images were taken at the Baylor College of Medicine Cryo-Electron Microscopy Core Facility (Texas Medical Center, Houston, TX). 3 μl of sample were loaded onto Quantifoil holey carbon grids (Quantifoil Micro Tools GmbH, Jena, Germany) and imaged with a 200kV JEOL Model 2200 Electron Microscope (JEOL Ltd, Japan) outfitted with an in-column Energy Filter. Images were captured using a Direct Electron DE20 direct detection device (Direct Electron, San Diego, CA) and the image capturing software SerialEM (Boulder, CO). Stability of PNPs was assessed in PBS at 37 °C over a period of 7 days, by daily measurements of size distribution by DLS.

2.5. Drug loading and release quantification

DCTXL loading and release were measured by HPLC (ThermoFisher, Ultimate 3000) equipped with a C18 column and UV detector at 227 nm, with 1 mL/min flow rate using acetonitrile and water (50:50) as mobile phase. DOXO was quantified by UV spectroscopy (Perkin Elmer, Lambda 365) at 480 nm in water/acetonitrile (50:50). For drug release, PNPs (1 mg/ml) were suspended in phosphate buffer (PBS, pH 7.4). At predetermined time intervals, the suspension was centrifuged and the supernatant was collected and analyzed by HPLC followed by UV analysis.

Encapsulation Efficiency (EE) was determined according to the following equation (Eq. (1)):

$$EE = D/D^{*} \times 100 \quad (1)$$

where D^{*} is the amount of drug initially supplied, and D is the amount of the drug quantified in the batch. Drug release data were fitted according to the Korsmeyer-Peppas equation using the SigmaPlot software (Systat Software Inc.) to calculate the equation parameters.

2.6. SPIOs loading

Samples were acid-digested in a Start D microwave-assisted digestion system (Milestone – Sorisole, BG, Italy). An aliquot of 1 mg of each sample was weighed and put in a PTFE vessel with 4 mL of 69% nitric acid and 4 mL of ultrapure water (Merck Millipore, Darmstadt, Germany). Iron content analysis was performed with a Thermo Scientific X Series 2 ICP-MS (Thermo Fisher Scientific – Waltham, MA, USA) equipped with a PFA micro-flow concentric nebulizer. Analyses were carried out in CCT-KED mode. Quantitative analysis were performed by means of calibration standard solutions in the range of 0.1–100.0 μg/L. Iron 1000 μg/mL stock solution was purchased by Inorganic Ventures (Christiansburg, VA, USA). Instrumental data were elaborated by PlasmaLab software, version 2.6.1.335.

2.7. Cell internalization and cytotoxicity studies

U-87 MG cells (Sigma Aldrich) were maintained in eMEM, supplemented with 10% FBS and 1% Penicillin/streptomycin. Cells were plated at 10,000 cells/well and cultured for 24 h. The medium was then substituted with 200 μL of PNPs suspension (empty nanoparticles, single drug-loaded PNPs, dual drug loaded PNPs and free drugs) in complete medium at different concentration and incubated for 24 h and 48 h. Cell viability was determined by Calcein Am assay, according to the manufacturer's instructions. Cell internalization of rhodamine-labelled empty PNPs was visualized by Fluo ViewTM 1000 confocal microscope (Nikon). Briefly U87 cells were incubated with PNPs (0.5 mg/mL) for 2 h, fixed in formalin for 20 min, washed three times with sterile PBS and stained by DAPI to visualize the nuclei. For the quantification of particle internalization, cells were washed 3 times with sterile PBS to remove particles that were not internalized, detached from the plate, centrifuged and washed 2 extra times with sterile PBS. Untreated cells were used as controls. Cells were analyzed by BD Accuri C6-Plus flow cytometer, using R-phycoerythrin (PE) laser (Ex/Em. 496/578) and recording 80.000 events per sample (n = 3).

2.8. Relaxometric analysis

In vitro T_1- and T_2-weighted MR relaxation studies were performed in 2% agar phantoms, using a clinical 3T scanner (GE Excite HDXt from GE Healthcare®, USA). The longitudinal (T1) relaxation time was obtained using inversion recovery pulse sequence (Repetition Time (TR) = 5000 ms; field of view (FOV) = 16 × 16 cm; number of excitations = 2, 224x224; Echo Time (TE) = 8.52 ms; Inversion times (TI) = 50, 100, 300, 500, 700, 900, 1100, 1300, 1500, 1700, 1900, 2100, 2300 ms), while the transverse (T_2) relaxation time was measured using a T_2 map Spin Echo pulse sequence (acquisition parameters: TR = 5000 ms; FOV = 16 × 16 cm; number of excitations = 2, 224x224; TE = 7, 14, 21, 28, 35, 42, 49, 56, 63, 70, 77, 84, 91, 100, 107, 114 ms) at different PNPs concentrations (0.14; 0.07; 0.03 mM equivalent Fe content). Transverse relaxivity (r_2) and longitudinal relaxivity (r1) values were estimated by the slope of the regression curve, according to the following equation (Eq. (3)):

$$R_i - R_{i-AGAR} = r_i * C, \quad i = 1,2 \tag{3}$$

where R_i (= $1/T_1$) is the relaxation rate and C is the nanoparticles concentration.

2.9. Photoacoustic imaging

Photoacoustic (PA) and ultrasound (US) measurements were performed with VevoLAZR system (FUIJIFILM VisualSonics Inc.). Samples were excited with a Nd:YAG laser (6–8 ns pulse width, 20 Hz) with an optical parametric oscillator from 680 to 950 nm. The laser illumination is transferred to the sample by a PA-US probe consisting of a Piezoelectric Linear Array (PLA) echography transducer (13–24 MHz with FOV of 23 × 30 mm). The PNPs behavior was studied in *in vitro* and *ex vivo* setups. The in vitro PA custom-made phantom is composed by a cubic polypropylene (PP) box and PE tubes loaded with the PNPs. We tested 3 PNPs concentrations in PBS (0.75 mg/mL; 1.5 mg/mL; 3.0 mg/mL). PBS alone was used as blank. For the ex vivo setup, tissue samples of approx. 30 × 15 × 10 mm were placed inside the PP box, covered with agarose (1% w/v) at 36 °C, and sonicated for 15 min. Before the PA acquisitions, 150 μL from PNPs stock solution (3 mg/mL) were injected, the system was filled with water and analyzed to evaluate photo-stability (PHS) and spectral PA response. The PA values were calculated into selected regions of interest (ROI) of the same size. The Spectral PA response analysis (PAS) was performed using a laser stimulation (2 nm step, 26 mJ of maximum energy peak) in the range 680–950 nm. The PHS was evaluated over 1 min (300 laser shots) under pulsed irradiation at 770 nm. The stability (i.e. the PA signal intensity over time) was studied under continuous laser stimulation by calculating the percentage difference between the value acquired during the first and the last 3 s of PHS acquisitions. The contrast-to-noise ratio (CNR) and Contrast were assessed in post processing [24]. Details for the calculation of these parameters are reported in the supplementary information paragraph.

2.10. Biodistribution analysis

For biodistribution analysis, CW-800 labelled nanoparticles were intravenously injected and mice were sacrificed at different time-points post-injection (3 h, 6 h, 24 h; 3 mice/group) through cardiac puncture. Organs were harvested and analyzed by IVIS imaging to evaluate the qualitative dynamics of uptake and clearance. Fluorescence in organs and blood was quantified by measuring the fluorescence spectra of homogenized organs using a Synergy H4 Hybrid Microplate Reader (BioTek) (Excitation Wavelength 745 nm, Emission Wavelength 780 nm). Collected organs were homogenized with a T25 Digital Ultra Turrax Homogenizer (Ika; 25 × 10^3 rpm; 1 min/organ) in PBS. Plasma was separated from whole blood by centrifugation (10 min, 3000g). Organ homogenates from pristine mice were used to normalize the results. Biodistribution was also evaluated in tumor-bearing mice for the best performing PNP platform. Briefly, Balb/C mice (3 groups of 3 mice each) were sub-cutaneous injected with luciferase-transfected 4T1 breast cancer cells (100.000 cells). Once the tumors reached a similar luminescence signal (detected by IVIS imaging and reported as supplementary Fig. 1), mice were injected i.v. with CW-800-labelled empty PU80 PNPs (group 1), co-loaded PU80 PNPs (group 2), and a combination of the two un-encapsulated drugs (group 3) at a final concentration of 3 mg/kg for both drugs. Mice from group 1 were imaged after 3 h, 6 h and 24 h by live imaging system IVIS and PNPs distribution was evaluated at the 24 h time point as described above in blood, organs, and tumor explants. Tumor explants from group 2 and group 3 mice were homogenized, the drugs were extracted form tissue homogenates and quantified by fluorescence reading (Ex/Em. 470/550) for Doxorubicin HC and by HPLC at 227 nm for DCTXL [25,26].

2.11. Statistical analysis

Results are expressed as mean ± standard deviation calculated using Microsoft Excel (Redmond, WA, USA) software. Statistical analysis was performed using Prism GraphPad software. One-way ANOVA followed by the post hoc analysis (Tukey) was used to compare the results. A p value of less than 0.05 was considered as statistically significant.

3. Results

3.1. Characterization of nanoparticles – surface properties

PURs with the desired structure were successfully obtained, as demonstrated by ATR-FTIR spectra (supplementary Fig. 2a) that show the stretching vibration of the –NH groups (3300–3400 cm^{-1}), the CH2 groups (2850–2970 cm^{-1}), and the stretching vibrations of the –C–O–C– and the carbonyl groups of the PCL segments (1190 cm^{-1} and 1723 cm^{-1}). For PEG-containing PURs, an additional signal at 1110 cm^{-1} associated with the stretching of –C–O–C– of the ether groups in the PEG segments was detected. All PURs have similar molecular weights, ranging from 4.6*10^4 to 5.3*10^4, with a low dispersity, as shown in Table 1 and by SEC traces, reported in supplementary Fig. 2b.

PNPs with small size and with the desired core-shell structure were obtained by nano precipitation self-assembly method, regardless of the choice of the PUR core, as confirmed by TEM (Fig. 2a) and by DLS measurements (Table 1). Size, PDI and zeta potential were similar among the tested platforms, and spherical PNPs with small diameters ranging from 95 to 140 nm, depending on the polymer composition, and a negative surface charge were obtained.

The presence of hydrophilic blocks in the polyurethane soft segment resulted in enhanced polydispersity index (PDI) and in reduced size of the PNPs prepared by the nanoprecipitation self-assembly method. We assumed this was due to the affinity between PEG and water that reduced the interaction between the polymer core and the stabilizing phospholipid outer shell during nanoprecipitation. For instance, we also synthesized PURs with a 40% ratio between PEG and PCL (PU60) but could not achieve a stable particle structure with this polymer, as demonstrated by the high PDI and by the biphasic DLS profile of PU 60 PNPs shown in supplementary Fig. 3. For this reason, a maximum amount of PEG of 30% in the PUR composition could be inserted to obtain

Table 1
Molecular weight and polydispersity (D) of PURs. Size, PDI and Zeta potential or PUR PNPs.

Material	PUR composition		PUR characterization		PUR PNPs characterization		
	PCL (%)	PEG (%)	Mw (Da)	D	Size (nm)	PDI	Z-Potential (mV)
PU 70	70	30	4.6 x 10^4	1.44	95 ± 6	0.3 ± 0.003	−57 ± 0.7
PU 80	80	20	5.2 x 10^4	1.42	101 ± 3	0.3 ± 0.006	−76 ± 0.7
PU 100	100	0	4.6 x 10^4	1.28	143 ± 5	0.2 ± 0.003	−73 ± 2.2

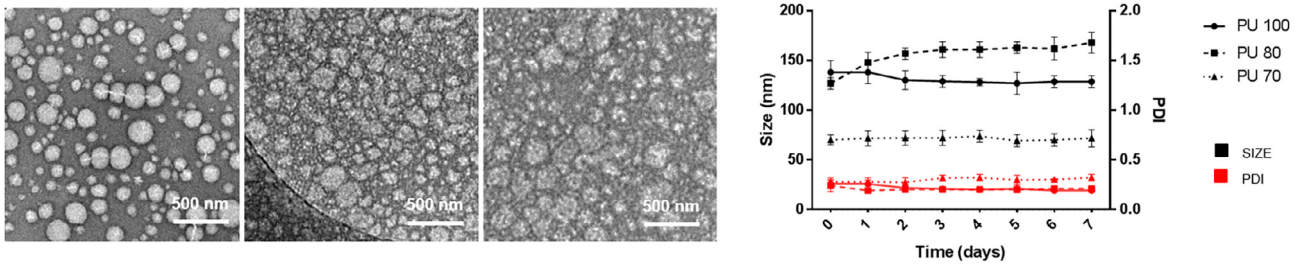

Fig. 2. a) TEM analysis of PU100, PU80, and PU70 PNPs (scale bars represent 500 nm); b) PNPs stability curve over 7 days of incubation in saline, evaluated as a daily measurement of size (black curves) and PDI (red curves). (For interpretation of the references to colour in this figure legend, the reader is referred to the web version of this article.)

stable particles with low PDI with the selected nanoprecipitation method.

All PUR PNPS showed good stability in normal saline (Fig. 2b) as demonstrated by the unaltered size and PDI over the tested period of 7 days, and did not elicit evident signs of toxicity on in vitro cell cultures up to a concentration of 1 mg/mL (supplementary Fig. 4c). We also evaluated the extent of rhodamine-labelled PNPs internalization by cancer cells in vitro, which is known to be dependent on the surface properties of the carriers. Rhodamine-labelled PNPs showed a similar internalization profile (Fig. 3a) regardless of the PUR composition. The particles were quickly internalized by cancer cells, due to the cell membrane-friendly phospholipid shell, and appeared to be mainly localized in the cytoplasm, as evidenced by the red fluorescence of rhodamine around the nuclei. Z-stack images, taken at higher magnifications (supplementary Fig. 4b) confirmed the location of the particles inside the cells. The uptake of nanoparticles was high for all platforms, ranging from 64 ± 4% for PU100 to 72 ± 1% for PU70 PNPs (Fig. 3b), confirming similar uptake profiles among carriers.

Because stability, toxicity and cell uptake are mainly surface-dependent properties, the above results suggest that the surface of PNPs was not altered by the use of different PUR cores.

To further support this statement we also evaluated the biodistribution profiles in vivo on Balb/c mice after 3 h, 6 h, and 24 h from tail vein injection (Fig. 4).

As expected, all particles accumulated preferentially in the liver and kidneys, through which they are excreted and were eliminated from circulation within 24 h from injection, as shown by the sharp decrease in fluorescence concentration in the blood at the 24 h time point [27,28]. Because all platforms share similar surface charge, surface composition, stability and size, no significant difference was observed in biodistribution profiles among PUR PNPs.

These results support our hypothesis that particles of similar size with the same surface compartment, behave similarly in vitro and in vivo.

3.2. Characterization of nanoparticles – bulk properties

Properties that are dependent on the PUR composition, such as drug entrapment efficiency, release profile and cytotoxicity, are reported in Table 2 for single agent platforms (i.e. PUR PNPs loaded with one agent at the time) and for co-loaded platforms (PUR PNPs containing the three payloads). The presence of the hydrophilic PEG domains clearly enhanced the encapsulation efficiency (EE) of the hydrophilic DOXO ($p = 0.0002$).

In multiple-agent platforms DOXO encapsulation was significantly higher (~30%) for the hydrophilic PURs as compared to the hydrophobic PU100 (~20%) ($p = 0.032$ and $p = 0.045$ for PU70 vs PU100 and PU80 vs PU100, respectively). When compared to other platforms for DOXO or DCTXL delivery, single-agent loaded PUR PNPs displayed a 1.1–2.3 fold higher DOXO EE, and a 1.2–4.8 fold higher DCTXL EE. Notably, when 3 agents were co-loaded in PUR PNPs, the EE of the drugs was still higher than or comparable to the EE values obtained in literature, thus confirming the potential of PUR PNPs as drug loading devices able to host multiple payloads [9,29–31]. Fig. 5a shows the cumulative release profiles of DOXO and DCTXL from PUR PNPs. As expected, the release of the hydrophilic drug was fast from all platforms, given the high affinity of the payload for the external aqueous environment, and was completed after 48 h of incubation. DCTXL release profile was more controlled over time for all 3 PNPs, with a slower release rate from PU100 PNPs. The release kinetic of DCTXL was similar for all PNPs (Fig. 5a) and characterized by a burst release in the first hours, followed by a constant release probably due to diffusion of DCTXL from PNPs and to a partial erosion of the particle. DCTXL-loaded-PLA/PLGA-NPs prepared by Musumeci et al displayed a similar biphasic release profile, but a much higher initial burst effect of about 40% to 68% within the first sampling time (24 h) [31]. In terms of in vitro cytotoxicity, all PUR PNPs showed similar results (Fig. 5b). In vitro drug release curves were fitted according to the Korsmeyer-Peppas model ($M_t/M_\infty = Ktn$) where M_t/M_∞ indicates the fraction of drug released at time t, k is the release rate constant and n is the release exponent, which is correlated with the drug release mechanism [32]. The values of the constant k, summarized in supplementary Fig. 5, are lower than 0.45 for all PUR PNPs, which correspond to a Fickian diffusion mechanism.

Cytotoxicity graphs for free drugs and single agent-PNPs, reported in supplementary Fig. 6, show that both drugs have strong cytotoxic effect on U87 in vitro. After 48 h of incubation, the IC50 of free DCTXL and free DOXO were 3.13 μg/ml and 1.59 μg/ml, respectively. Encapsulated DCTXL and DOXO maintained similar IC50 values, ranging respectively from 5.19 μg/ml and 2.69 μg/ml for PU100; 0.91 μg/ml and 1.31 μg/ml for PU80; and 4.78 μg/ml and 1.88 μg/ml for PU70. The combined platforms showed IC50 as low as 1 μg/ml for combined drugs after 48 h of incubation. No significant differences were observed among platforms, in accordance with their similar release profiles.

The encapsulation efficiency of SPIOs did not vary significantly among platforms, particularly when SPIOs were co-loaded with DCTXL and DOXO (Table 2). These results indicate that the presence of PEG did not affect the entrapment efficiency of hydrophobic SPIOs, but affected the superparamagnetic behavior of PNPs. Fig. 6a summarizes the relaxometric properties in terms of longitudinal (r1) and transversal (r_2) relaxivities. All platforms showed high r_2 values, ranging from 25.86 ± 13.02 $(mM\ s)^{-1}$ for PU70, 27.33 ± 8.58 $(mM\ s)^{-1}$ for PU80 and 20.98 ± 7.23 $(mM\ s)^{-1}$ for PU100. Encapsulated SPIOs showed a typical superparamagnetic behavior, which was not affected by the polymer coating [33]. The presence of PEG domains significantly affected the MRI contrast enhancement, confirming that hydrophilic coatings improve the magnetic response of SPIOs (Fig. 6b) [34]. Indeed, proton relaxation of paramagnetic systems has been shown to depend mainly

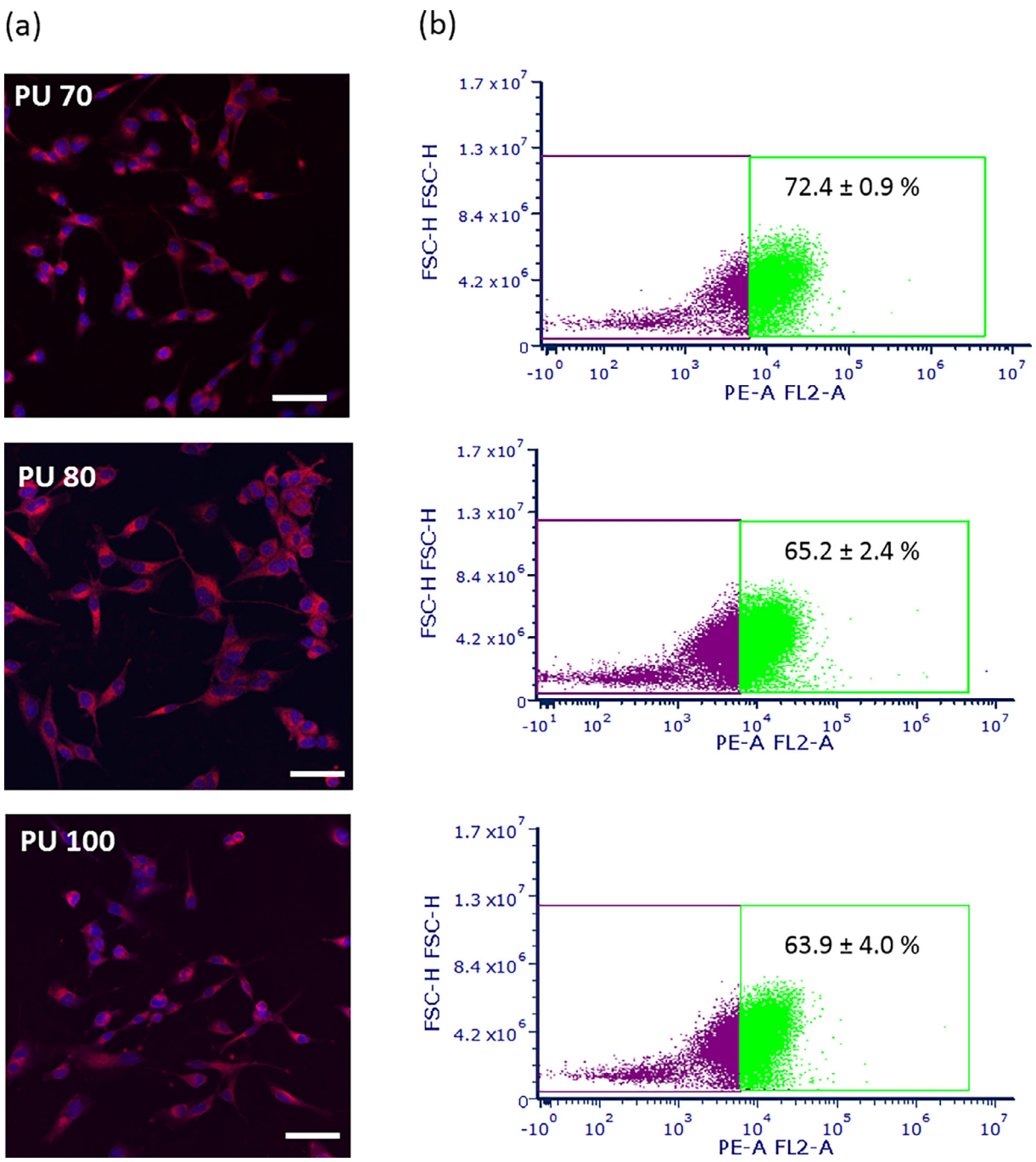

Fig. 3. a) Internalization of PUR PNPs by U87 glioblastoma cancer cells in vitro. Rhodamine-labelled, drug-free PNPs appear in red, nuclei were stained with DAPI (scale bars correspond to 50 μm); b) Quantification of cell internalization by flow cytometry. Green: percentage of rhodamine-positive cells, purple: percentage of negative cells. (For interpretation of the references to colour in this figure legend, the reader is referred to the web version of this article.)

on the water protons movement near the local magnetic field [35]. Thus, for PU70 and PU80 PNPs that contain hydrophilic PEG domains, interactions with water protons were favored.

On the other hand, the hydrophobic PU100 PNPs had lower interaction between water protons and encapsulated SPIOs, resulting in a lower transversal response. The r_2/r_1 ratio of SPIOs-loaded PNPs, which is a measure of the contrast-enhancement efficiency of the system, was also dependent on the PEG content, ranging from 27 ± 1 for PU 70, 26 ± 7 for PU 80, and 15 ± 6 for PU 100. Considering that commercial T_2 contrast agents typically possess a r_2/r_1 ratio in the range between 2 and 40, and that commercially-available agents such as Resovist, Feridex and Combidex have a r_2/r_1 ratio <14.1, the values obtained for all PUR PNPs warrant their further investigation as T_2-contrast agents in MRI [36,37].

PA performance of PUR PNPs are summarized in Fig. 7 and in Table 3. All PUR PNPs exhibit comparable PA spectra profiles and signal intensities both in our in vitro (PE tubes) and ex vivo (tissue phantoms) setups. The in vitro photostability (PHS) of the surface-immobilized dye was very high for all tested PNP (supplementary Fig. 7), while the dye alone showed high variability in signal intensity over the tested period of time. PUR PNPs displayed a significantly higher PA signal when compared to the semiconducting self-assembled polymer-based nanoprobes developed by Xie and coworkers and by Pu et al [38–40].

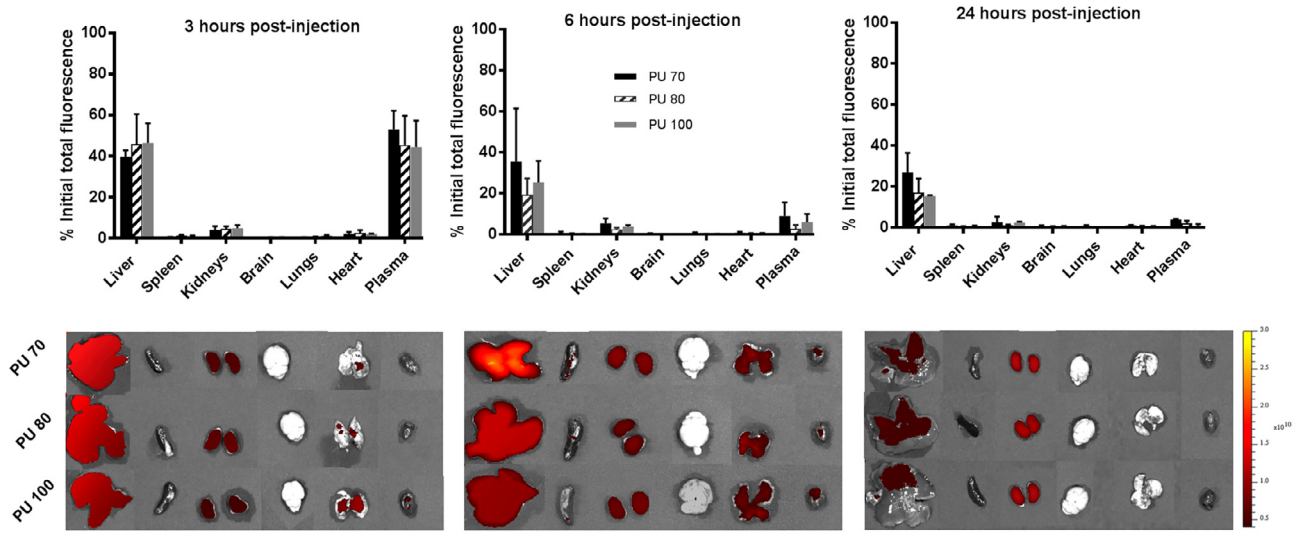

Fig. 4. Biodistribution profile of PUR PNPs. Quantification of fluorescence in extracted organs at different time points (upper panel), and IVIS imaging of extracted organs (one representative mouse per polyurethane for each time point).

Table 2
Encapsulation efficiency of PUR PNPs when used as multiple-agent loading platforms or as a single-agent loading platform. Physico-chemical characterizations of single-agent loaded PUR PNPs are reported in supplementary Table 1.

Material	Single-agent platforms			Co-loaded platforms		
	EE $_{Doxo}$ (%)	EE $_{Dctxl}$ (%)	Fe [ppm]	EE $_{Doxo}$ (%)	EE $_{Dctxl}$ (%)	Fe [ppm]
PU 70	45.2 ± 4.7	43.8 ± 6.2	4844 ± 737	31.0 ± 4.8	15.8 ± 0.5	4602 ± 203
PU 80	44.8 ± 1.3	48.2 ± 6.0	5545 ± 308	30.1 ± 3.5	17.5 ± 1.1	4671 ± 80
PU 100	22.3 ± 0.5	22.0 ± 2.7	7607 ± 1282	19.6 ± 3.2	13.2 ± 1.5	5860 ± 174

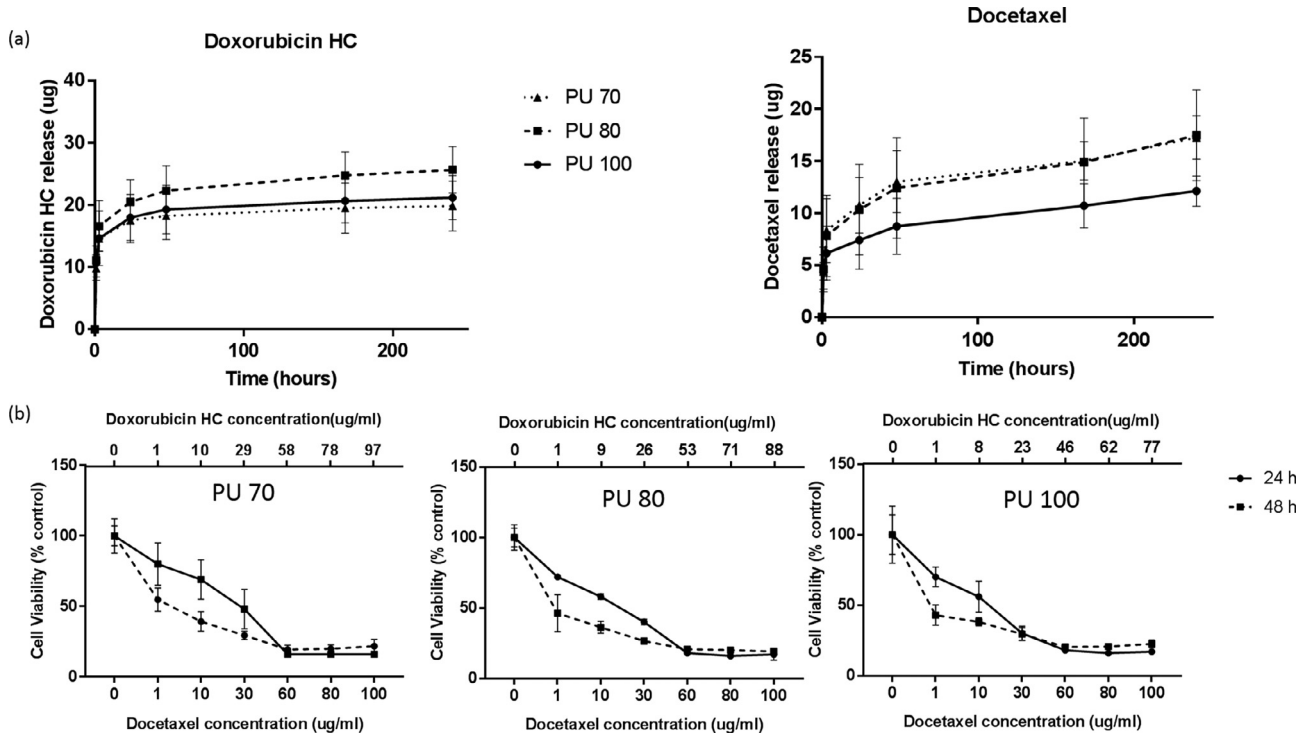

Fig. 5. Drug release profiles (a) and cytotoxicity profiles (b) of PUR PNPs.

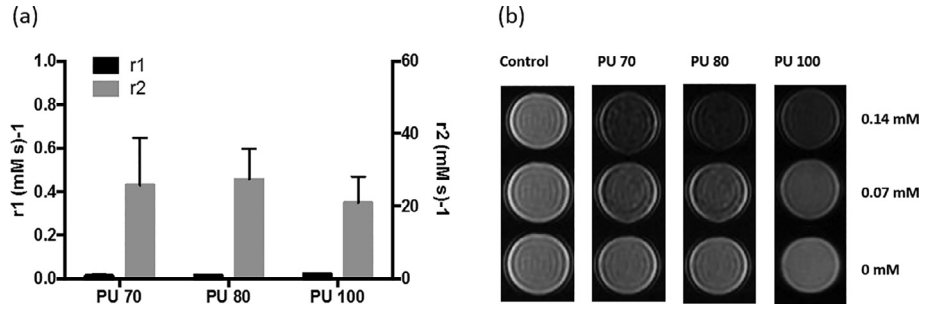

Fig. 6. Relaxometric properties of PNPs. Transversal (r_2) and longitudinal (r1) relaxivity for all platforms (a). Dose-dependent (mM Fe equivalent) contrast enhancement on agar phantoms (b).

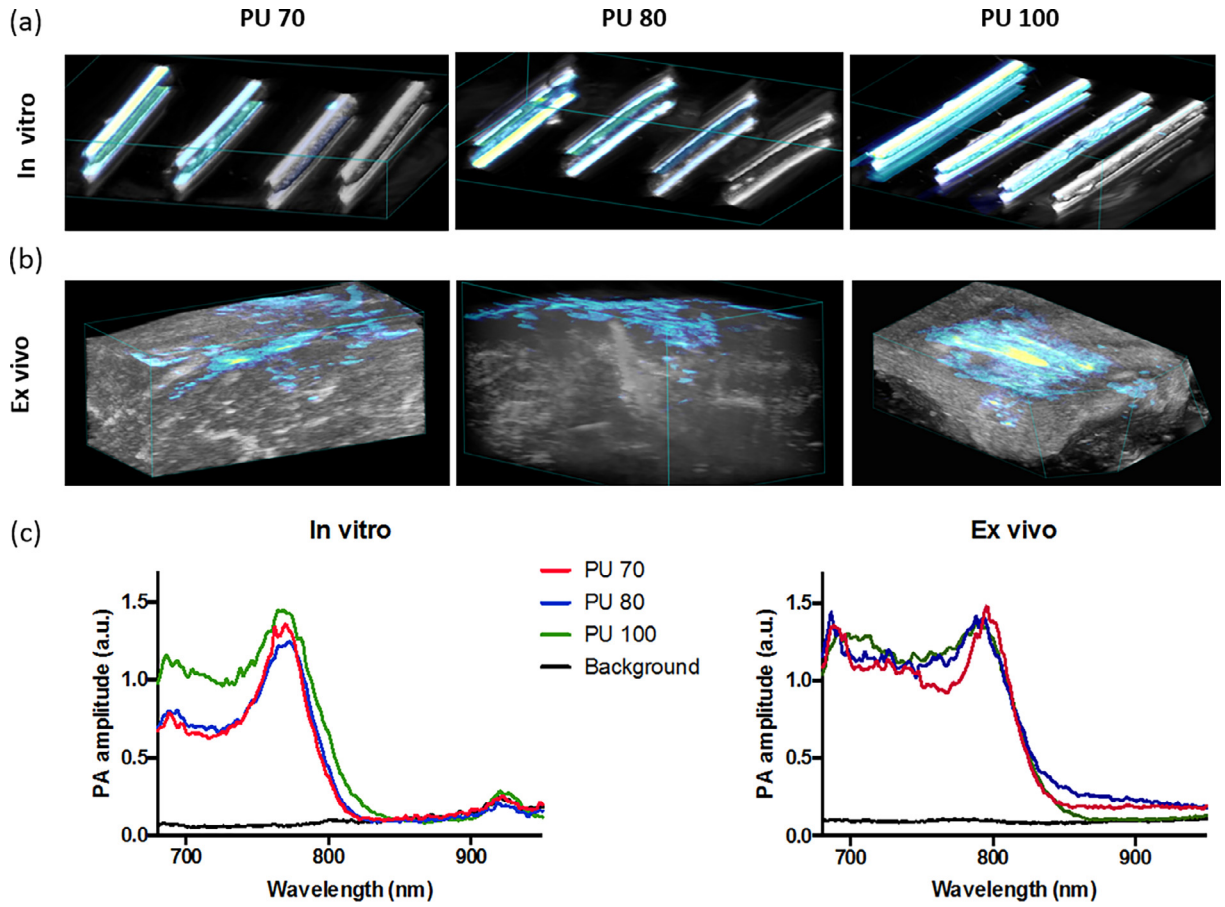

Fig. 7. PA properties of PNPs. a) 3D renders of PA-US distribution of different PNPs concentration at 770 nm loaded in PE tubes, b) *Ex vivo* phantom results: 3D render of PA distribution of PNPs (600 μg/ml) perfusion inside the tissue of phantom after the injection, c) Spectra of CW-800 modified PNPs (600 μg/ml), measured in the in vitro set up and in the ex vivo 3D phantom.

Table 3
PA performances derived from PUR PNPs after *phantom* and *ex vivo* tests.

Material	In vitro			Ex vivo		
	PA (770 nm)	CNR	Contrast	PA	CNR	Contrast
PU 70	1.3	45.6	21.4	1.5 ± 0.2	30	9
PU 80	1.2	40.7	18.3	1.1 ± 0.1	76	11
PU 100	1.4	89.9	18.1	2.2 ± 0.1	67	16

3.3. Tumor accumulation ability of PUR PNPs

Given that all PNPs behaved similarly in terms of circulation properties and cell internalization kinetics, we selected the best-performing PUR PNP (PU80) platform in terms of higher drug entrapment efficiency, sustained release profile, MRI contrast enhancement, and PA imaging performances and injected it into tumor-bearing mice to investigate the passive tumor targeting ability. Fig. 8a, and c show the biodistribution of PU80 PNPs in tumor-bearing mice. After 24 h from the injection, a high PNP dose accumulated in the tumor (5.1 ± 2.1% of the injected dose), while 7.5 ± 4.3% remained in the liver.

When loaded with DOXO and DCTXL, the particles significantly enhanced drug co-delivery to tumor as compared to free drugs (Fig. 8b). A 15-fold increase in tumor accumulation of DOXO vs free drug was obtained with PNPs, while a 1.6-fold increase was achieved for DCTXL. The ratio between DOXO and DCTX in tumor

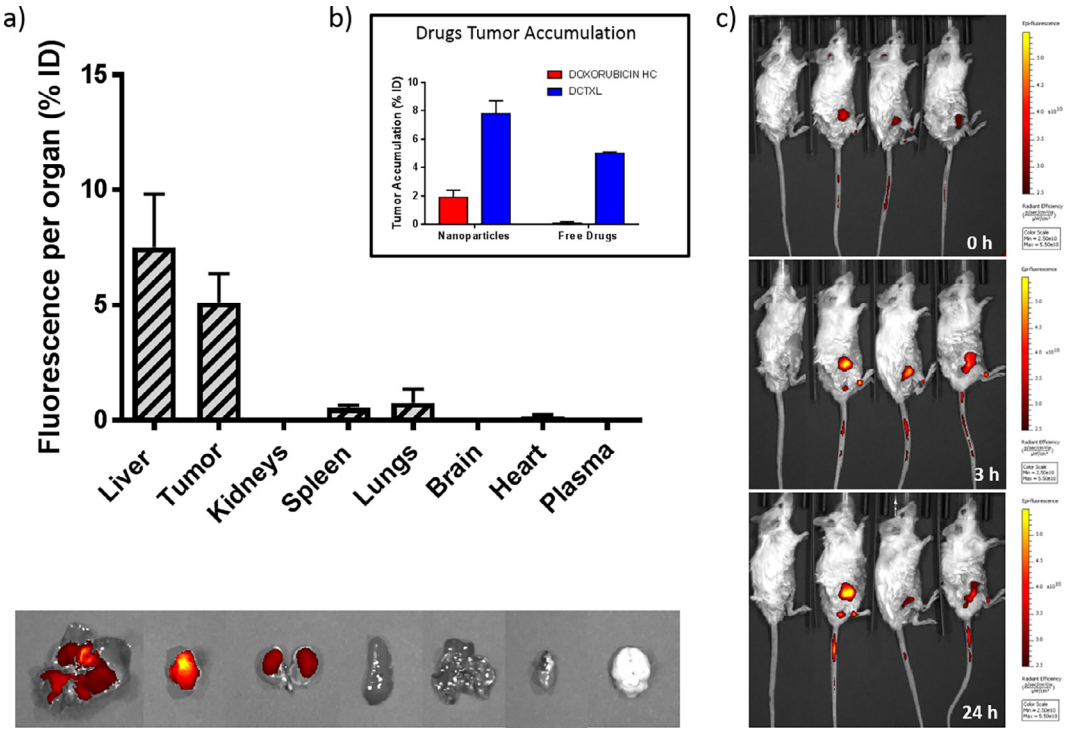

Fig. 8. Biodistribution of PUR 80 PNPs after tail vein injection in tumor-bearing mice. a) Quantification of fluorescence in extracted organs after 24 h; b) drugs quantification in the extracted tumors for nanoparticles-injected and free drugs-injected mice; c) in vivo circulation of nanoparticles imaged by IVIS system at different time points.

was 0.3 ± 0.01 for the co-loaded platform, almost 11 fold higher than that achieved with free drugs.

4. Discussion

Combination of chemotherapeutics is a valuable strategy to improve patient outcome and to overcome drug resistance. Unfortunately, different drugs may have different delivery routes and chemical/physical properties, resulting in un-matching pharmacokinetics and tumor accumulation profiles and in the loss of the synergistic effect [3]. Because of their ability to passively or actively accumulate into tumors, polymer nanoparticles have been proposed to package different molecules in a single polymer core in order to enhance their co-delivery [6]. While co-encapsulation of hydrophobic drugs has been achieved with success, the combination of hydrophilic and hydrophobic drugs remains an issue, as it requires polymer platforms with high affinity for both molecules [3,9].

In this work we used the tunable chemistry of poly(ester-ether) urethanes (PURs) containing hydrophobic (PCL) and hydrophilic (PEG) blocks at different ratio (100/0; 80/20 and 70/30) to increase affinity for both, hydrophilic and hydrophobic drugs. We previously showed that PUR PNPs have higher entrapment efficiency of hydrophobic drugs and display more sustained delivery as compared to traditional polyester PNPs [11,41]. We have attributed this high PUR/drug interaction to the semi-crystalline nature of PURs and to the presence of amorphous domains in their microstructure [42]. In this work we demonstrate that the insertion of PEG blocks in the PUR soft segment composition results in higher entrapment efficiency of DOXO, while DCTXL encapsulation did not depend on the soft segment composition and remained high among all tested platforms. When PUR PNPs were co-loaded with 3 agents (2 drugs and SPIOs as MRI contrast agents), the EE of the drugs was higher than or comparable to the EE values obtained in literature for single-agent PNPs, thus confirming the potential of PUR PNPs as drug loading devices able to host multiple payloads. Yoo and co-workers reported DOXO-loaded polymeric micelles with an EE of ~20%, while Dessy et al obtained DOXO EE in the range 23–26% using the poly(ether-ester-urethane) nanoparticles [29,30]. For DCTXL, EE values ranging from 10 to 25% were reported by Musumeci et al. for PLA/PLGA-NPs, and by Decuzzi and co-workers for PLGA PNPs [9,31]. The presence of PEG also played a role in enhancing the MRI contrast enhancement, in spite of similar SPIOs EE of the three PUR PNPs. This was attributed to the favored PUR matrix hydrations and to the consequent interaction between entrapped SPIOs and water protons that has been reported to enhance the contrast effect in MRI. We showed that modulation of the polymer core properties is a promising strategy to co-load drugs with different physical properties and pharmacokinetics.

One other important issue in designing particles for drug delivery is the effect of the polymer matrix on the surface properties of the carriers that strongly affect cell interaction, in vivo biodistribution and tumor accumulation of PNPs [17,18]. To reduce the effects of the different polymer on the surface properties of the carriers, we opted for a core/shell particle design, in which PURs constitute the core and can be modified to favor entrapment of different compounds, and the surface is conceived to remain un-altered and is composed of a mixture of phospholipids and PEGylated phospholipids.

Our results showed that this PNP design favors cell internalization and results in similar biodistribution profiles. All particles showed long circulation time, accumulated mainly in the liver due the low blood velocity in this organs that favors PNPs uptake by macrophages, and were excreted through the kidneys, as widely reported for particles of this size and surface charge [27]. No significant differences in biodistribution or in vitro cell uptake were observed among platforms, indicating that the surface properties of the carriers remained un-altered. In tumor-bearing mice, PU80 PNPs showed high passive tumor accumulation, with more than 5 % of the 5 injected dose accumulating in tumors after 24 h.

Moreover, PUR PNPs efficiently co-delivered the two drugs at the target site. We observed a 15-fold increase in DOXO accumulation in tumors as compared to free drug. Only a small amount of DOXO was detected in tumors of mice treated with un-encapsulated drugs, coherently with previous reports that indicate DOXO clearance within few minutes from injection [15]. We also detected a 1.6 fold higher DCTXL content in tumor for encapsulated drugs as compared to free drugs. The ratio between the two drugs delivered through the co-loaded platform was 11-fold higher than that obtained for free drugs, indicating that the proposed particle design can improve drug accumulation and also can efficiently co-localize chemotherapeutics with different pharmacokinetics.

5. Conclusions

In this work, PNPs were prepared using PURs containing different percentages of hydrophilic domains (0%, 20% and 30%) as the particle's core, and a specific composition of phospholipids as the outer shell. The versatility of the outer shell was also exploited for photoacoustic/fluorescent imaging purposes, with high efficiency. This approach resulted in good modulation of the drug encapsulation efficiency without negatively influencing circulation time, biodistribution, cellular uptake, and stability, which are known surface-dependent properties. Efficient tumor co-localization of drugs with different physical/chemical properties was achieved through modulation of the hydrophilic/hydrophobic balance of PURs. These findings evidence the advantages of using tunable polymers for PNPs and suggest further investigation on the use of tailor made PURs in nanomedicine.

Acknowledgements

The authors would like to acknowledge Dr. Attilio Marino and Dr. Gianni Ciofani, at the Department of Smart Bio-Interfaces, Italian Institute of Technology for confocal imaging support; and the Preclinical Imaging Core of Houston Methodist Hospital Research Institute for service of IVIS Spectrum System.

This project has received funding from the European Union's Horizon 2020 research and innovation programme under the Marie Sklodowska-Curie grant agreement No 658665, and by the "Fondazione Cassa di Risparmio di Pisa" through the project "PREVISION".

Appendix A. Supplementary data

Supplementary data to this article can be found online at https://doi.org/10.1016/j.actbio.2018.09.021.

References

[1] E. Blanco, Nanoparticle-based polychemotherapy: optimizing drug synergy for efficacious cancer treatment, Ther. Delivery 5 (7) (2014) 737–739.
[2] K. Kim, J.H. Kim, H. Park, Y.S. Kim, K. Park, H. Nam, S. Lee, J.H. Park, R.W. Park, I. S. Kim, K. Choi, S.Y. Kim, K. Park, I.C. Kwon, Tumor-homing multifunctional nanoparticles for cancer theragnosis: simultaneous diagnosis, drug delivery, and therapeutic monitoring, J. Control Release 146 (2) (2010) 219–227.
[3] E. Blanco, T. Sangai, S. Wu, A. Hsiao, G.U. Ruiz-Esparza, C.A. Gonzalez-Delgado, F.E. Cara, S. Granados-Principal, K.W. Evans, A. Akcakanat, Y. Wang, K.A. Do, F. Meric-Bernstam, M. Ferrari, Colocalized delivery of rapamycin and paclitaxel to tumors enhances synergistic targeting of the PI3K/Akt/mTOR pathway, Mol. Ther.: J. Am. Soc. Gene Ther. 22 (7) (2014) 1310–1319.
[4] N. Kolishetti, S. Dhar, P.M. Valencia, L.Q. Lin, R. Karnik, S.J. Lippard, R. Langer, O. C. Farokhzad, Engineering of self-assembled nanoparticle platform for precisely controlled combination drug therapy, Proc. Natl. Acad. Sci. U.S.A. 107 (42) (2010) 17939–17944.
[5] J. Shi, Z. Xiao, N. Kamaly, O.C. Farokhzad, Self-assembled targeted nanoparticles: evolution of technologies and bench to bedside translation, Acc. Chem. Res. 44 (10) (2011) 1123–1134.
[6] E. Blanco, H. Shen, M. Ferrari, Principles of nanoparticle design for overcoming biological barriers to drug delivery, Nat. Biotechnol. 33 (9) (2015) 941–951.
[7] D. Cassano, J. David, S. Luin, V. Voliani, Passion fruit-like nano-architectures: a general synthesis route, Sci. Rep. 7 (2017) 43795.
[8] Y. Mi, C. Mu, J. Wolfram, Z. Deng, T.Y. Hu, X. Liu, E. Blanco, H. Shen, M. Ferrari, A micro/nano composite for combination treatment of melanoma lung metastasis, Adv. Healthcare Mater. 5 (8) (2016) 936–946.
[9] C. Stigliano, J. Key, M. Ramirez, S. Aryal, P. Decuzzi, Radiolabeled polymeric nanoconstructs loaded with docetaxel and curcumin for cancer combinatorial therapy and nuclear imaging, Adv. Funct. Mater. 25 (22) (2015) 3371–3379.
[10] C. Mattu, R.M. Pabari, M. Boffito, S. Sartori, G. Ciardelli, Z. Ramtoola, Comparative evaluation of novel biodegradable nanoparticles for the drug targeting to breast cancer cells, Eur. J. Pharm. Biopharm. 85 (3) (2013) 463–472.
[11] C. Mattu, M. Boffito, S. Sartori, E. Ranzato, E. Bernardi, M.P. Sassi, A.M. Di Rienzo, G. Ciardelli, Therapeutic nanoparticles from novel multiblock engineered polyesterurethanes, J. Nanopart. Res. 14 (12) (2012).
[12] C. Mattu, A. Silvestri, T.R. Wang, M. Boffito, E. Ranzato, C. Cassino, G. Ciofani, G. Ciardelli, Surface-functionalized polyurethane nanoparticles for targeted cancer therapy, Polym. Int. 65 (7) (2016) 770–779.
[13] C. Mattu, T.R. Wang, A. Siri, S. Sartori, G. Ciardelli, Ionic cross-linking of water-soluble polyurethane improves protein encapsulation and release, Eng. Life Sci. 15 (4) (2015) 448–455.
[14] A.A. van der Veldt, N.H. Hendrikse, E.F. Smit, M.P. Mooijer, A.Y. Rijnders, W.R. Gerritsen, J.J. van der Hoeven, A.D. Windhorst, A.A. Lammertsma, M. Lubberink, Biodistribution and radiation dosimetry of 11C-labelled docetaxel in cancer patients, Eur. J. Nucl. Med. Mol. Imaging 37 (10) (2010) 1950–1958.
[15] R. Luo, Y. Li, M. He, H. Zhang, H. Yuan, M. Johnson, M. Palmisano, S. Zhou, D. Sun, Distinct biodistribution of doxorubicin and the altered dispositions mediated by different liposomal formulations, Int. J. Pharm. 519 (1–2) (2017) 1–10.
[16] M.T. Sheu, H.J. Jhan, C.Y. Su, L.C. Chen, C.E. Chang, D.Z. Liu, H.O. Ho, Codelivery of doxorubicin-containing thermosensitive hydrogels incorporated with docetaxel-loaded mixed micelles enhances local cancer therapy, Colloids Surf. B Biointerfaces 143 (2016) 260–270.
[17] T. Sun, Y.S. Zhang, B. Pang, D.C. Hyun, M. Yang, Y. Xia, Engineered nanoparticles for drug delivery in cancer therapy, Angew. Chem. Int. Ed. Engl. 53 (46) (2014) 12320–12364.
[18] S. Vrignaud, J.P. Benoit, P. Saulnier, Strategies for the nanoencapsulation of hydrophilic molecules in polymer-based nanoparticles, Biomaterials 32 (33) (2011) 8593–8604.
[19] C. Iodice, A. Cervadoro, A.L. Palange, J. Key, S. Aryal, M.R. Ramirez, C. Mattu, G. Ciardelli, B.E. O'Neill, P. Decuzzi, Enhancing photothermal cancer therapy by clustering gold nanoparticles into spherical polymeric nanoconstructs, Opt. Laser Eng. 76 (2016) 74–81.
[20] S. Mallidi, G.P. Luke, S. Emelianov, Photoacoustic imaging in cancer detection, diagnosis, and treatment guidance, Trends Biotechnol. 29 (5) (2011) 213–221.
[21] J.L. Su, B. Wang, K.E. Wilson, C.L. Bayer, Y.S. Chen, S. Kim, K.A. Homan, S.Y. Emelianov, Advances in clinical and biomedical applications of photoacoustic imaging, Expert Opin. Med. Diagn. 4 (6) (2010) 497–510.
[22] C. Avigo, A. Flori, P. Armanetti, N. Di Lascio, C. Kusmic, J. Jose, P. Losi, G. Soldani, F. Faita, L. Menichetti, Strategies for non-invasive imaging of polymeric biomaterial in vascular tissue engineering and regenerative medicine using ultrasound and photoacoustic techniques, Polym. Int. 65 (7) (2016) 734–740.
[23] I. Monaco, F. Arena, S. Biffi, E. Locatelli, B. Bortot, F. La Cava, G.M. Marini, G.M. Severini, E. Terreno, M. Comes Franchini, Synthesis of lipophilic core-shell Fe3O4@SiO2@Au nanoparticles and polymeric entrapment into nanomicelles: a novel nanosystem for in vivo active targeting and magnetic resonance-photoacoustic dual imaging, Bioconjug Chem. 28 (5) (2017) 1382–1390.
[24] M.S. Patterson, F.S. Foster, The improvement and quantitative assessment of B-mode images produced by an annular array/cone hybrid, Ultrason. Imaging 5 (3) (1983) 195–213.
[25] M. Rezazadeh, J. Emami, A. Mostafavi, M. Rostami, F. Hassanzadeh, H. Sadeghi, M. Minaiyan, A. Lavasanifar, A rapid and sensitive hplc method for quantitation of paclitaxel in biological samples using liquid-liquid extraction and UV detection: application to pharmacokinetics and tissues distribution study of paclitaxel loaded targeted polymeric micelles in tumor bearing mice, J. Pharm. Pharm. Sci. 18 (5) (2015) 647–660.
[26] K. Alhareth, C. Vauthier, C. Gueutin, G. Ponchel, F. Moussa, HPLC quantification of doxorubicin in plasma and tissues of rats treated with doxorubicin loaded poly(alkylcyanoacrylate) nanoparticles, J. Chromatogr. B Anal. Technol. Biomed. Life Sci. 887–888 (2012) 128–132.
[27] S.M. Moghimi, J. Szebeni, Stealth liposomes and long circulating nanoparticles: critical issues in pharmacokinetics, opsonization and protein-binding properties, Prog. Lipid Res. 42 (6) (2003) 463–478.
[28] M. Cataldi, C. Vigliotti, T. Mosca, M. Cammarota, D. Capone, Emerging role of the spleen in the pharmacokinetics of monoclonal antibodies, nanoparticles and exosomes, Int. J. Mol. Sci. 18 (6) (2017).
[29] H.S. Yoo, K.H. Lee, J.E. Oh, T.G. Park, In vitro and in vivo anti-tumor activities of nanoparticles based on doxorubicin-PLGA conjugates, J. Control Release 68 (3) (2000) 419–431.
[30] A.P.A. Dessy, M. Alderighi, S. Sandreschi, F. Chiellini, Doxorubicin loaded polyurethanes nanoparticles, Nano Biomed. Eng. 4 (2) (2012) 6.
[31] T. Musumeci, C.A. Ventura, I. Giannone, B. Ruozi, L. Montenegro, R. Pignatello, G. Puglisi, PLA/PLGA nanoparticles for sustained release of docetaxel, Int. J. Pharm. 325 (1–2) (2006) 172–179.

[32] S. Dash, P.N. Murthy, L. Nath, P. Chowdhury, Kinetic modeling on drug release from controlled drug delivery systems, Acta Polym. Pharm. 67 (3) (2010) 217–223.
[33] M. Khalkhali, K. Rostamizadeh, S. Sadighian, F. Khoeini, M. Naghibi, M. Hamidi, The impact of polymer coatings on magnetite nanoparticles performance as MRI contrast agents: a comparative study, Daru 23 (2015) 45.
[34] N. Lee, T. Hyeon, Designed synthesis of uniformly sized iron oxide nanoparticles for efficient magnetic resonance imaging contrast agents, Chem. Soc. Rev. 41 (7) (2012) 2575–2589.
[35] S. Laurent, D. Forge, M. Port, A. Roch, C. Robic, L. Vander Elst, R.N. Muller, Magnetic iron oxide nanoparticles: synthesis, stabilization, vectorization, physicochemical characterizations, and biological applications, Chem. Rev. 108 (6) (2008) 2064–2110.
[36] M.F. Casula, A. Corrias, P. Arosio, A. Lascialfari, T. Sen, P. Floris, I.J. Bruce, Design of water-based ferrofluids as contrast agents for magnetic resonance imaging, J. Colloid Interface Sci. 357 (1) (2011) 50–55.
[37] G. Shahnaz, C. Kremser, A. Reinisch, A. Vetter, F. Laffleur, D. Rahmat, J. Iqbal, S. Dunnhaupt, W. Salvenmoser, R. Tessadri, U. Griesser, A. Bernkop-Schnurch, Efficient MRI labeling of endothelial progenitor cells: Design of thiolated surface stabilized superparamagnetic iron oxide nanoparticles, Eur. J. Pharm. Biopharm. 85 (3) (2013) 346–355.
[38] C. Xie, X. Zhen, Y. Lyu, K. Pu, Nanoparticle regrowth enhances photoacoustic signals of semiconducting macromolecular probe for in vivo imaging, Adv. Mater. 29 (44) (2017).
[39] K. Pu, A.J. Shuhendler, J.V. Jokerst, J. Mei, S.S. Gambhir, Z. Bao, J. Rao, Semiconducting polymer nanoparticles as photoacoustic molecular imaging probes in living mice, Nat. Nanotechnol. 9 (3) (2014) 233–239.
[40] C. Xie, P.K. Upputuri, X. Zhen, M. Pramanik, K. Pu, Self-quenched semiconducting polymer nanoparticles for amplified in vivo photoacoustic imaging, Biomaterials 119 (2017) 1–8.
[41] S. Sartori, V. Chiono, C. Tonda-Turo, C. Mattu, C. Gianluca, Biomimetic polyurethanes in nano and regenerative medicine, J. Mater. Chem. B 2 (32) (2014) 5128–5144.
[42] X. Guo, D. Li, G. Yang, C. Shi, Z. Tang, J. Wang, S. Zhou, Thermo-triggered drug release from actively targeting polymer micelles, ACS Appl. Mater. Interfaces 6 (11) (2014) 8549–8559.